Journal of Physics D: Applied Physics

PAPER

Infrared study of plasmon–phonon coupling in pure and Nd-doped CeO_{2-y} nanocrystals

To cite this article: M Radovi *et al* 2015 *J. Phys. D: Appl. Phys.* **48** 065301

IOP Publishing Journal of Physics D: Applied Physics

J. Phys. D: Appl. Phys. **48** (2015) 065301 (8pp) doi:10.1088/0022-3727/48/6/065301

Infrared study of plasmon–phonon coupling in pure and Nd-doped CeO_{2-y} nanocrystals

M Radović[1], Z Dohčević-Mitrović[1], N Paunović[1], S Bošković[2], N Tomić[1] N Tadić[3] and I Belča[3]

[1] Center for Solid State Physics and New Materials, Institute of Physics, University of Belgrade, 11080 Belgrade, Serbia
[2] Institute for Nuclear sciences 'Vinča', Materials Science Laboratory, University of Belgrade, Belgrade, Serbia
[3] Faculty of Physics, University of Belgrade, 11000 Belgrade, Serbia

E-mail: marrad@ipb.ac.rs

Received 9 October 2014, revised 12 December 2014
Accepted for publication 23 December 2014
Published 22 January 2015

Abstract

Plasmon-longitudinal-optical (LO) phonon interaction in pure and Nd-doped CeO_{2-y} nanocrystals was investigated by measuring far–infrared reflectivity spectra in the 100–700 cm^{-1} spectral range at room temperature. Analysis of the obtained results revealed that the presence of free charge carriers becomes significant with the particle size decrease to nanometer range and increase of lattice defects. The free charge carriers were found to be responsible for a plasmon mode which coupled strongly with two LO phonon modes of ceria. The presence of more pronounced low-frequency Drude tail and the screening of the phonon modes in Nd-doped CeO_{2-y} nanocrystals implied that the Plasmon-LO phonon interaction increased with doping. Factorized and additive dielectric function models were applied to deduce about the coupled and decoupled LO phonon frequencies and the structure of the decoupled plasmon mode in pure and Nd-doped CeO_{2-y} nanocrystals. These models were combined with Bruggeman effective medium approximation in order to properly describe the influence of porosity on the infrared reflectivity spectra. With increasing dopant content, the decoupled plasmon mode exhibited redshift and damping decrease implying that doping induced semiconductor–to–metalic state transition took place.

Keywords: Nd-doped ceria nanocrystals, infrared spectroscopy, plasmon–phonon interaction

(Some figures may appear in colour only in the online journal)

1. Introduction

Cerium dioxide (CeO_2, ceria) is a wide band gap semiconductor with ionic and partially covalent bonding nature [1, 2], which has received considerable interest due to the variety of applications in advanced technologies. CeO_2-based solid solutions have been acknowledged to be the most promising electrolytes for intermediate temperature solid oxide fuel cells, exhibiting excellent ionic conductivity at intermediate temperatures (500 – 800° C) [3, 4], much better than traditional ionic conductors like yttria-stabilized zirconia [3]. With a reduction of particle size, ceria becomes a mixed ionic–electronic conductor [5], because the presence of defects and unsaturated surface bonds leads to the increase of the free carrier contribution to the overall conductivity. The electrical conductivity of nanocrystalline ceria based materials can be attributed to the small polaron hopping mechanism [6, 7]. It was shown [8, 9] that the electrical conductivity, measured at different temperatures and oxygen partial pressures, is increased with the decreasing size of nanoparticles and is almost 10^4 times greater than in microcrystalline materials [8, 9]. This property can be utilized for gas sensor applications [10].

The influence of free carrier collective excitations (plasmons) on the optical phonon spectra of nanocrystalline ceria, i.e. plasmon–phonon coupling, has not been studied. The infrared (IR) spectroscopy is a nondestructive and widely applied spectroscopic technique for the investigation of the

mechanism of plasmon–phonon coupling in different materials. From the IR reflection spectra of polar semiconductors, both phonon and plasmon excitations can be registered, enabling the direct investigation of the plasmon – phonon interaction mechanism.

In the present paper, the plasmon – phonon interaction in pure and Nd-doped CeO_{2-y} nanocrystals has been investigated by analyzing the IR reflection spectra of these samples. The application of factorized and additive forms of the dielectric function, together with Bruggeman effective medium approximation, allowed the determination of coupled (decoupled) phonon frequencies, damping parameters and the structure of decoupled plasmon mode with doping. Better insight into the plasmon – phonon coupling mechanism in nanocrystalline ceria can be very important because the plasmon – phonon interaction can influence the ceria electrical conductivity properties.

2. Experimental

Undoped CeO_{2-y} nanopowders were prepared using the self-propagating room temperature synthesis and the detailed preparation procedure is described elsewhere [11, 12]. The as-prepared samples were calcinated at 600 and 800° C for 2 h, in order to induce the growth of crystalite size. The Nd-doped samples were doped with 10, 15, 20 and 25 wt% Nd. X-ray diffraction (XRD) technique was used for the characterization of structural properties and the degree of crystallinity of the synthesized nanopowders. Diffraction patterns were recorded over the 2θ range from 20 to 80° on a Siemens D-5000 diffractometer, using Cu Kα radiation The external standard correction was performed using LaB_6 (NIST) powder. Atomic force microscope (AFM) images were taken using the Omicron B002645 SPM PROBE VT AFM 25 in noncontact mode. The IR reflectivity spectra were measured at room temperature in the far-IR region (100–700 cm^{-1}) on a Bomem DA8 spectrometer using the DTGS detector.

3. Models

In this section, a brief overview of the theoretical models used to analyze the measured IR spectra will be presented.

The IR reflectivity spectra of the ionic crystals where large splitting between transverse-optical (TO) and longitudinal-optical (LO) modes is observed [13, 14], are usually fitted with a dielectric function given by the expression [15]:

$$\varepsilon_M = \varepsilon_\infty \prod_j \frac{\omega_{\mathrm{LO}j}^2 - \omega^2 + \mathrm{i}\omega\gamma_{\mathrm{LO}j}}{\omega_{\mathrm{TO}j}^2 - \omega^2 + \mathrm{i}\omega\gamma_{\mathrm{TO}j}}, \tag{1}$$

where ε_∞ is the high frequency dielectric constant and $\omega_{\mathrm{TO(LO)}j}$ and $\gamma_{\mathrm{TO(LO)}j}$ are the TO and LO phonon frequencies and damping rates of the corresponding IR mode. This model introduces four adjustable parameters for each TO-LO mode and is used for description of pure phonon properties. In further text it will be named the Lattice Vibrations model (LV). The main disadvantage of this model results from the fact that it does not take into account the contribution from the electronic excitations i.e. the plasmons and plasmon–phonon coupling.

Most semiconductors have a significant portion of free carriers and a complete description of the far-IR optical properties of semiconductor materials has to take both phonon and plasmon contributions into account. The coexistence of phonons and plasmons usually leads to a strong coupling between plasmons and LO phonons. This effect is most pronounced when the plasma frequency (ω_P) is in the vicinity of the LO phonon frequency. In that case the plasmon–phonon interaction can be described with the factorized form of the dielectric function given by [16, 17]:

$$\varepsilon_M = \varepsilon_\infty \frac{\prod_{j=1}^{m+n}\left(\omega^2 + \mathrm{i}\omega\gamma_{\mathrm{LO}j} - \omega_{\mathrm{LO}j}^2\right)}{\omega^m \prod_{j=1}^{m}\left(\omega + \mathrm{i}\gamma_{Pj}\right)\prod_{j=1}^{n}\left(\omega^2 + \mathrm{i}\omega\gamma_{\mathrm{TO}j} - \omega_{\mathrm{TO}j}^2\right)}, \tag{2}$$

where ω_{TOj} and γ_{TOj} are frequencies and damping rates of the TO modes and γ_P is the plasma damping. This expression gives directly the coupled plasmon-LO phonon frequencies ω_{LOj} and damping rates γ_{LOj} and in further text will be named as the Coupled Plasmon – Phonon (CPP) model.

The extension of the Drude model which has been used to fit the IR reflectivity spectra of conducting oxides is known in the literature as the Double-damping extended Drude model [18]. The additive form of the dielectric function in which the plasmon contribution is expressed by Double-damped Drude term, is composed of two terms:

$$\varepsilon_M = \varepsilon_\infty \left(\prod_j \frac{\omega_{\mathrm{LO}j}^2 - \omega^2 + \mathrm{i}\omega\gamma_{\mathrm{LO}j}}{\omega_{\mathrm{TO}j}^2 - \omega^2 + \mathrm{i}\omega\gamma_{\mathrm{TO}j}} - \frac{\omega_P^2 + \mathrm{i}(\gamma_P - \gamma_0)\,\omega}{\omega\left(\omega - \mathrm{i}\gamma_0\right)} \right). \tag{3}$$

The first term represents the phonon contribution and the second term is the plasmon contribution. The $\omega_{\mathrm{TO(LO)}j}$ and $\gamma_{\mathrm{TO(LO)}j}$ are TO(LO) frequencies and dampings of decoupled phonon modes, whereas the ω_P, γ_P and γ_0 are the plasma frequency and dampings at $\omega = \omega_P$ and $\omega = 0$. This model allows the decoupling of phonon and plasmon contributions and enables to make a difference between the damping (γ_P) at the plasma frequency and the static damping at zero frequency (γ_0). The second term in equation (3) becomes the classical Drude formula for $\gamma_P = \gamma_0$. The application of this model offers more flexibility in numerical fitting and more precise description of the dielectric function response [18]. In further text this model will be named the Decoupled Plasmon – Phonon (DPP) model.

In order to properly analyze the IR spectra of porous nanomaterials, one of the most commonly used models is the Bruggeman effective medium approximation [19, 20]. For the inhomogeneous, binary material, composed of material (ε_M) and air ($\varepsilon_{\mathrm{air}} = 1$) with the volume fractions f_M and $1 - f_M$ respectively, the empirical relation for the effective dielectric function ($\varepsilon_{\mathrm{eff}}$) can be written as [20]:

$$\left(\frac{\varepsilon_M - \varepsilon_{\mathrm{eff}}}{\varepsilon_M + 2\varepsilon_{\mathrm{eff}}}\right) f_M + \left(\frac{1 - \varepsilon_{\mathrm{eff}}}{1 + 2\varepsilon_{\mathrm{eff}}}\right)\left(1 - f_M\right) = 0. \tag{4}$$

Therefore, the effective dielectric function (ε_{eff}) from equation (4) of a pure and Nd-doped CeO_{2-y} porous nanocrystalline sample can be expressed in terms of the dielectic function of material (ε_M) given by equations (1), (2) or (3) and volume fractions of material and air.

The theoretical reflectivity is obtained by using the Fresnel formula:

$$R_{\text{calc}} = \left| \frac{\sqrt{\varepsilon_{\text{eff}}} - 1}{\sqrt{\varepsilon_{\text{eff}}} + 1} \right|^2 . \quad (5)$$

The least-squares fitting procedure between the theoretical (R_{calc}) and experimental (R_{exp}) reflectivity was carried out until the chi-squared value:

$$\chi^2 = \frac{1}{N} \sum_{i}^{N} \left(R_{i,\text{exp}} - R_{i,\text{calc}} \right)^2 \quad (6)$$

was minimized, where N is the number of measured points.

4. Results and discussion

A detailed analysis of the XRD spectra of undoped and Nd-doped samples has been already given in [11, 12]. The Nd-doped samples crystallized into a fluorite type structure of CeO_2 with Nd^{3+} ions entering substitutionally into a ceria lattice. The presence of amorphous or any other phase was not detected, even for the highest Nd concentration [11, 12]. The synthesized samples were composed of very small particles in the nanometric range (3–4 nm) [11, 12]. Additionally, the undoped CeO_{2-y} sample was calcinated at 600 and 800°C for 2 h in air, in order to compare the structural and vibrational properties of thermally treated and non-treated samples. The XRD spectra of thermally treated samples are given in figure 1(*a*). Characteristic Miller indices are denoted for main diffraction peaks. The average crystallite size and strain values were calculated using the Williamson–Hall method [21, 22] and the obtained values for each sample are presented in figure 1(*a*). In the inset of figure 1(*a*) is presented the Williamson–Hall plot of an as-prepared CeO_{2-y} sample. The calcinated samples exhibited sharper diffraction lines as a consequence of increased crystallite size and much better degree of crystallinity. The XRD pattern of the sample calcinated at 800°C is similar to the XRD spectrum of polycrystalline CeO_2. In figures 1(*b*) and (*c*) are presented AFM images of a ceria sample calcinated at 800°C and of an as-prepared CeO_{2-y} sample. The size of nanocrystals was in good agreement with the average crystallite size obtained from the XRD data.

Bearing in mind that ceria phonon properties are very much dependent on the crystallite size, we first investigated the influence of the particle size on the infrared reflectivity spectra of as-prepared and calcinated samples of CeO_{2-y}. In figure 2 are presented the IR reflectivity spectra of a bulk CeO_2 sample (reconstructed according to the literature data [2]) and calcinated ceria samples with different crystallite sizes, determined from XRD spectra from figure 1. Factor-group analysis for a fluorite type CeO_2 structure, predicts only one triple-degenerate IR active phonon mode of the F_{2u} symmetry, with TO and LO mode frequencies at 218 and 597 cm^{-1}, respectively [2]. In the IR spectrum of the bulk sample, wide reststrahlen band, characteristic for the ionic bond nature, is observed.

With decreasing crystallite size, the reststrahlen band splits into two broad TO-LO modes in the 200 – 550 cm^{-1} region. The splitting and redshift of both LO modes become more distinct in the sample with the smallest crystallite size (4.2 nm). A similar behavior was previously observed for pure and doped ceria powders [23] and for other nanostructured materials such as porous SiC films [20] and Mn_2O_3 nanocrystals [24]. It is reasonable to expect that the vibrational properties of nanomaterials are changed due to the increased concentration of structural defects (such as oxygen vacancies in ceria) and large number of dangling bonds at the nanoparticles surface, which leads to crystal symmetry breakdown. The lifting of the F_{2u} mode degeneracy in CeO_{2-y} nanocrystals can be ascribed to the long-range Coulomb field which splits the degeneracy of the polar modes in nanocrystals [24]. Another possible explanation for the observed splitting of the restrahlen band was ascribed to the multiphonon (anharmonic) effects [23].

From figure 2, for the CeO_{2-y} sample with the smallest crystallite size, it can be seen that the phonon modes are significantly damped and that the plasmonic background becomes prominent. The presence of lattice defects in the form of oxygen vacancies and consequently free charge carriers, is responsible for the appearance of the plasmonic background. The formation of an oxygen vacancy in the ceria lattice is followed by the localization of two electrons into empty Ce $4f^0$ orbitals [25], causing the change in the valence state of neighboring Ce ions from 4^+ to 3^+. With decreasing particle size, the concentration of oxygen vacancies increases. The electrons tend to be localized not only on the Ce sites, but also on the vacancy sites, giving rise to the formation of the *F*-center defect states [26, 27]. The electrons localized on vacancy sites behave like free charge carriers, which can significantly contribute to the increasing of ceria electrical conductivity as the crystallite size decreases [10]. Our previous Raman spectroscopy analysis of nonstoichiometric nanosized ceria [28] have demonstrated that anomalous broadening of the Raman F_{2g} mode can be ascribed to the electron-molecular vibrational coupling effect due to the increased concentration of charge carriers at the Fermi surface. It was shown that the delocalization of electrons onto oxygen vacancies causes semiconductor–to–metallic state transition in highly oxygen deficient nanosized ceria. Therefore, the electronic contribution to the dielectric function has to be properly taken into account in the analysis of the IR reflectivity spectra of the nanocrystalline CeO_{2-y} samples.

The IR reflectivity spectrum of CeO_{2-y} nanocrystals, with the smallest crystallite size (4.2 nm in figure 2), was analyzed using two models for plasmon – phonon interaction. The first one was the CPP model, (equation (2)), which enables to directly obtain coupled plasmon – phonon frequencies and dampings. The second one was the DPP model which was used to obtain the LO mode parameters of the decoupled phonons and plasmons, (equation (3)). These two models were

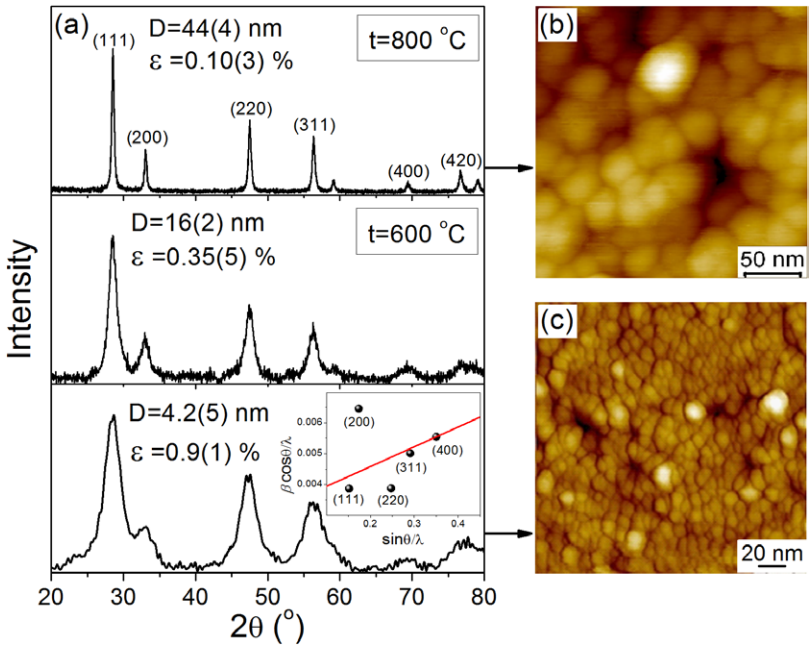

Figure 1. (*a*) XRD patterns of as-prepared and thermally treated CeO_{2-y}, together with the crystallite size (D) and strain (ε) values. The inset presents the Williamson–Hall plot of as-prepared CeO_{2-y}. AFM images of (*b*) CeO_{2-y} sample calcinated at 800°C and (*c*) as-prepared CeO_{2-y} sample.

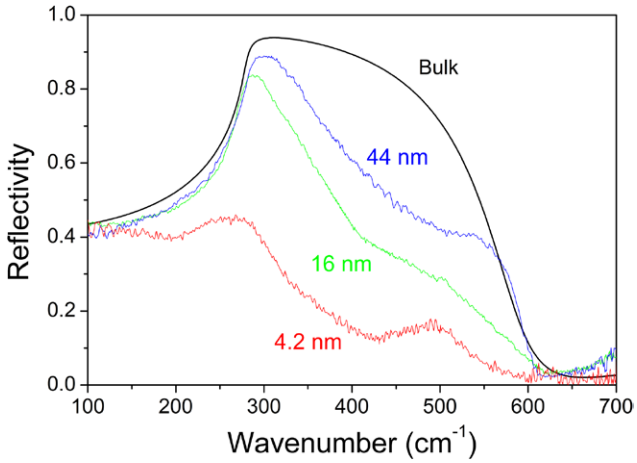

Figure 2. IR reflectivity spectra of CeO_{2-y} nanocrystals with different crystallite sizes and theoretical curve for bulk sample according to the data taken from [2].

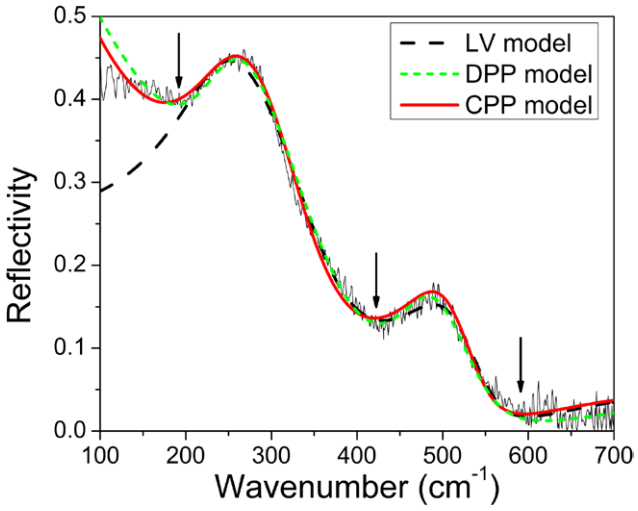

Figure 3. IR reflectivity spectrum of a CeO_{2-y} nanocrystalline sample (crystallite size 4.2 nm), together with theoretical fits using the LV, DPP and CPP models. The arrows mark the reflectivity minima.

combined with Bruggeman effective medium approximation (equation (4)) in order to properly include the influence of material porosity f_M on the resulting IR spectra. The dielectric function model which takes into account only the pure lattice vibrations (LV model given by equation (1)) was also applied. A comparison between the theoretical models and the experimental spectrum for a CeO_{2-y} sample is shown in figure 3. In all applied models, the reflectivity spectrum of the CeO_{2-y} sample was fitted with two oscillators (due to the observed splitting of the restsrahlen band).

From figure 3, it can be seen that LV model did not give a good fit of the experimental data in the frequency region bellow 200 cm^{-1}, because of the contribution of free charge carriers. On the contrary, both the CPP and DPP models gave satisfactory fits of the reflectivity data.

The plasmon-LO phonon coupling in the nanocrystalline CeO_{2-y} sample was analyzed by the CPP model, assuming that the plasmon mode is coupled with two LO phonon modes of the nanocrystalline CeO_{2-y} sample. In that case, the equation (2) becomes [17]:

$$\varepsilon_M = \varepsilon_\infty \frac{\left(\omega^2 - \omega_{LO1}^2 + i\omega\gamma_{LO1}\right)\left(\omega^2 - \omega_{LO2}^2 + i\omega\gamma_{LO2}\right)\left(\omega^2 - \omega_{LO3}^2 + i\omega\gamma_{LO3}\right)}{\omega\left(\omega + i\gamma_P\right)\left(\omega^2 - \omega_{TO1}^2 + i\omega\gamma_{TO1}\right)\left(\omega^2 - \omega_{TO2}^2 + i\omega\gamma_{TO2}\right)}. \quad (7)$$

From this model, the reflection spectrum minima occur for the eigenfrequencies ω_{LOj} (j = 1–3) [16], where the coupling between plasmon and two LO phonons manifests as the appearance of an additional longitudinal plasmon – phonon mode.

Table 1. Fitting parameters obtained by using the Coupled Plasmon–Phonon (CPP) model. The estimated errors are given in parenthesis.

Sample	f_M	γ_P	ω_{TO1}	γ_{TO1}	ω_{LO1}	γ_{LO1}	ω_{TO2}	γ_{TO2}	ω_{LO2}	γ_{LO2}	ω_{LO3}	γ_{LO3}	χ^2
	(±0.03)	(±10)	(±5)	(±10)	(±5)	(±15)	(±5)	(±10)	(±5)	(±15)	(±5)	(±15)	
CeO_{2-y}	0.8	210	248	120	370	155	492	105	545	75	210	290	0.0012
10%Nd	0.72	208	248	107	360	180	480	250	549	150	210	290	0.0013
15%Nd	0.61	118	240	176	336	110	477	210	552	190	185	205	0.001
20%Nd	0.56	90	244	95	343	165	480	130	546	110	193	108	0.0023
25%Nd	0.81	130	245	175	332	159	485	180	546	150	173	120	0.0041

Table 2. Fitting parameters obtained by using the Decoupled Plasmon–Phonon (DPP) model. The estimated errors are given in parenthesis.

Sample	f_M	ω_P	γ_P	γ_0	ω_{TO1}	γ_{TO1}	ω_{LO1}	γ_{LO1}	ω_{TO2}	γ_{TO2}	ω_{LO2}	γ_{LO2}	χ^2
	(±0.03)	(±5)	(±15)	(±15)	(±5)	(±10)	(±5)	(±15)	(±5)	(±10)	(±5)	(±15)	
CeO_{2-y}	0.8	450	360	330	245	100	300	45	479	100	505	75	0.0017
10%Nd	0.72	440	360	330	243	98	319	25	477	195	500	145	0.0015
15%Nd	0.61	315	289	151	243	190	273	78	475	190	515	110	0.001
20%Nd	0.56	310	180	83	246	97	299	110	475	110	515	107	0.0021
25%Nd	0.81	238	140	103	249	148	290	145	480	130	509	115	0.0042

In our case, this new mode, ω_{LO3}, corresponds to the reflection minimum at ~200 cm^{-1} in the reflectivity spectrum of the CeO_{2-y} sample. From the CPP model, the plasma frequency can be determined using the following equation [16, 17]:

$$\omega_P = \frac{\omega_{LO1}\omega_{LO2}\omega_{LO3}}{\omega_{TO1}\omega_{LO2}}, \tag{8}$$

and the frequencies of the coupled plasmon − phonon mode can be obtained by putting $\varepsilon_M = 0$ in the equation (7) [16, 17]:

$$\Omega_{LOj} = \sqrt{\omega_{LOj}^2 + \frac{1}{4}\gamma_{LOj}^2}\,. \tag{9}$$

The fitting parameters obtained from the CPP model, which yielded the best fit to the reflectivity spectrum for the CeO_{2-y} sample, are presented in table 1. The best fit parameters obtained from DPP model are presented in table 2. The values of plasma frequency (ω_P) and coupled plasmon–phonon modes (Ω_{LO1}, Ω_{LO2}) obtained from equations (8) and (9) are given in table 3. The value of the high frequency dielectric constant $\varepsilon_\infty = 4$, for nanocrystalline CeO_{2-y}, was used in both applied theoretical models. The reduced chi-squared values are given in the last column of tables 1 and 2.

From the fit parameters for the CeO_{2-y} sample, it can be concluded that the eigenfrequencies of the coupled (ω_{LO1} and ω_{LO2}) plasmon-LO phonon modes are shifted to higher energies with respect to the decoupled LO phonon frequencies (ω_{LO1} and ω_{LO2}). The frequency shift and increased damping of the coupled longitudinal modes can be assigned to the strong plasmon–phonon interaction. The TO frequencies of the corresponding modes are not affected by plasmon − phonon interaction, as expected.

Further, we investigated how Nd doping influences the plasmon–phonon interaction in CeO_{2-y} nanocrystals. In the IR refelectivity spectra of Nd-doped samples, presented in figure 4, the low frequency Drude tail and the screening of the phonon modes became pronounced. Therefore, the IR spectra of doped samples were fitted by using the CPP and

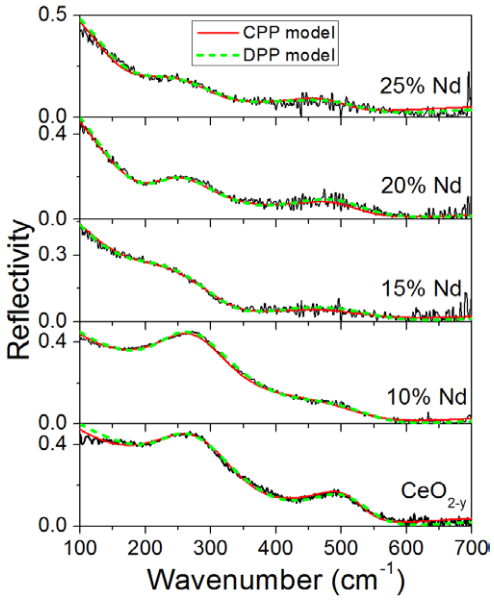

Figure 4. IR reflectivity spectra of pure and Nd-doped samples, together with theoretical fits obtained by CPP and DPP models.

DPP dielectric function models as previously in the case of the undoped CeO_{2-y} sample. In figure 4 are shown the IR reflectivity spectra of undoped and Nd-doped CeO_{2-y} nanocrystals together with theoretical fits obtained by the applied models.

The best fit parameters for Nd-doped samples, obtained from the CPP and DPP models, are given in tables 1 and 2. The materials volume fraction f_M decreased with Nd doping up to 20% of Nd, after which approaches the value for pure CeO_{2-y}. The estimated f_M is in good correlation with specific surface area (S_{BET}) measurements performed earlier on Nd-doped samples. It was found that doping with Nd cations had increased the porosity of ceria nanocrystals except for the sample doped with 25% of Nd for which the porosity decreased [12]. It is worth mentioning that the increased porosity can be also a reason for lower reflectivity of pure and

Table 3. Calculated values of the plasma frequency and coupled plasmon–phonon modes. The estimated errors are given in parenthesis.

Sample	ω_P	Ω_{LO1}	Ω_{LO2}
	(±5)	(±5)	(±5)
CeO_{2-y}	347	378	546
10%Nd	349	371	554
15%Nd	300	340	560
20%Nd	308	353	549
25%Nd	264	341	551

doped nanocrystalline ceria samples compared to the reflectivity of the bulk counterpart.

From the reflectivity spectra of Nd-doped samples it can be seen that with an increase of the dopant concentration (more than 10% of Nd) the low frequency Drude tail becomes more prominent and a pronounced screening of the phonon modes takes place. Such a behavior implies that with Nd doping the concentration of the free charge carriers increases. The presence of free charge carriers can be explained by the fact that with increasing Nd content in the ceria lattice, the number of oxygen vacancies increases. According to the paper of Han *et al* [26] in nonstoichiometric ceria, with increasing vacancy concentration the amount of electrons which are localized near the vacancy sites increases too, giving rise to the formation of *F*-center defects in different charge states ([27] and the references within). These electrons are loosely bound and behave more like free charge carriers. Additionally, in the paper of Chen and Wang [29] it was shown that in Nd-doped ZnO nanowires the formation of vacancies near the Nd cations, can induce an increase of concentration of free (delocalized) electrons. In a recent paper of Choudhury *et al* [30], using Hall effect measurements, it was demonstrated that in Nd-doped ceria nanopowders, with increasing Nd content up to 4%, the number of free carriers increased. The increased free carrier concentration caused the widening of the band gap due to Burstein–Moss shift. The above mentioned theoretical and experimatal works support our finding that the plasmon − phonon interaction in Nd-doped ceria samples become stronger.

By analyzing the fitting parameters of the doped samples from tables 1 and 2, we can see that TO frequencies are not much affected by doping, whereas the eigenfrequencies of the plasmon-LO phonon coupled modes (ω_{LO1} and ω_{LO2} from table 1) are notably shifted with respect to decoupled LO modes (ω_{LO1} and ω_{LO2} from table 2). It can be also noticed that the damping parameter γ_{LO1} is significantly increased for doped samples.

In figure 5(*a*) are presented the frequencies of the coupled plasmon–phonon modes (Ω_{LO1}, Ω_{LO2}) and the decoupled LO phonon modes (ω_{LO1} and ω_{LO2} from table 2) as a function of Nd content. From figure 5(*a*) it is obvious that frequencies of the coupled modes are shifted to higher energies. Since the plasma frequency ω_P in doped samples is much closer to the frequency of the Ω_{LO1} mode than to the frequency of the Ω_{LO2} mode (see table 3), it is expected that the plasmon–phonon coupling would be stronger for the Ω_{LO1} mode. The observed decrease of the Ω_{LO1} frequency with increasing Nd content confirms that this mode is more strongly coupled with plasmon.

In figure 5(*b*) is presented the variation of the plasma frequency ω_P with doping concentration in the case of both applied models. As can be seen from figure 5(*b*), we have obtained similar behavior of the plasma frequency from both models. The plasma frequency shifts towards lower energies as Nd concentration increases. Similar behavior of plasma frequency was found for crystalline and amorphous GaAs [31] when a metal-like phase appeared in these materials.

From the table 2 one can deduce that the plasmon mode is overdamped ($\gamma_P/\omega_P > 1/\sqrt{2}$) for the undoped CeO_{2-y} sample and samples doped up to 15% of Nd. This is a feature of conducting oxides, in particular cuprates [18]. For higher doping content (20 and 25% of Nd), the γ_P/ω_P ratio decreases ($\gamma_P/\omega_P \sim 0.5$). The decreasing trend of the γ_P/ω_P ratio is characteristic for the metallic state [18].

The plasmon dielectric function, according to the Double-damping extended Drude model, can be written in the form [18, 32]:

$$\epsilon_{pl} = \epsilon_\infty \left(1 - \frac{\omega_p^2 + i(\gamma_p - \gamma_0)\,\omega}{\omega\,(\omega - i\gamma_0)}\right) \tag{10}$$

The decoupled plasmon mode structure can be extracted from the imaginary part of the inverse plasmon dielectric function, $\mathrm{Im}(1/\epsilon_{pl})$ [32]. The decoupled plasmon mode structure with Nd doping is presented in figure 6, where the positions of the plasma frequencies (table 2) are marked with (*).

As can be seen from figure 6, with increased Nd doping the plasmon mode shifts towards lower energies, as well as the plasma frequency. The shift of the plasma frequency to lower energies is found in perovskite-type oxides like $BaPb_{1-x}Bi_xO_3$ [33] and $Ba_{1-x}K_xO_3$ [34], when these materials undergo semiconductor–to–metal transition. Bearing in mind that the plasma frequency ω_P is proportional to n_e/m^*, where n_e is the free carrier concentration and m^* is the electron effective mass, we can deduce that doping not only influences the free carrier concentration, but also changes the electron effective mass. In fact, our results for plasma frequency (plasmon mode) behavior suggest that the effective mass of free electrons increases with doping. Our conclusion is supported by the results performed on $Ba_{1-x}K_xO_3$ and InN films [34, 35] in which it was found a pronounced increase in the electron effective mass with increasing concentration of free carriers followed by a semiconductor–metal transition [34].

In order to verify how the plasmon–phonon interaction changes in thermally treated Nd-doped samples, the 15% and 25% Nd samples were calcinated in the same manner as it was done for the undoped ceria sample from figure 2. The IR refelectivity spectra of thermally treated 15% (25%) Nd-doped samples together with the corresponding untreated samples are presented in figure 7. As can be seen, the IR spectra of the calcinated samples are very similar to the bulk counterpart (figure 2), as the plasmonic background vanished and TO (LO) frequencies approached the bulk values. The disappearance of the Drude tail is expected, bearing in

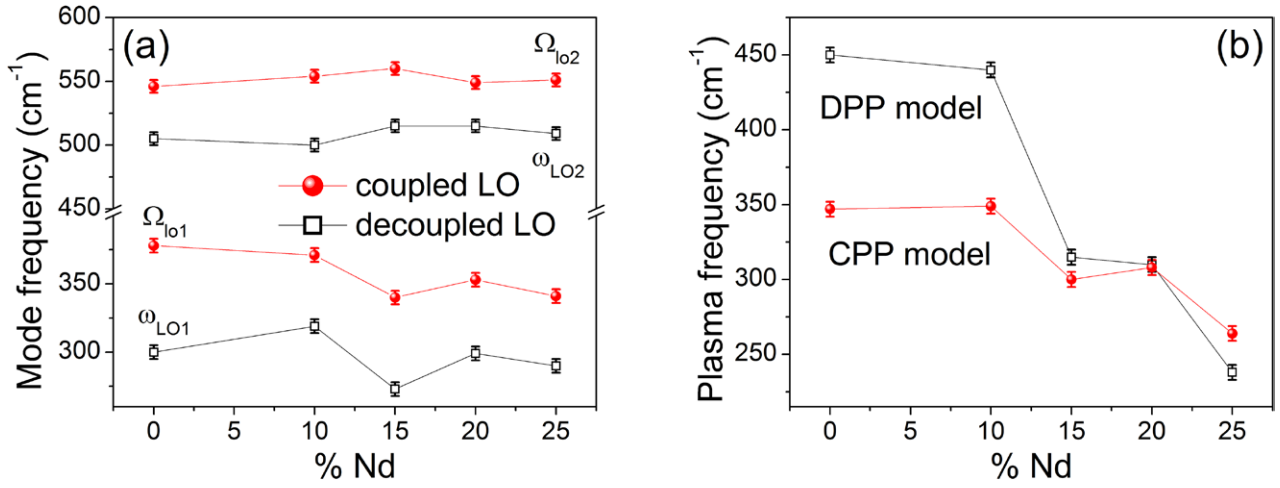

Figure 5. (*a*) Variation of the coupled and decoupled LO mode frequencies and (*b*) plasma frequency variation with Nd dopant concentration, obtained by using the CPP and DPP models.

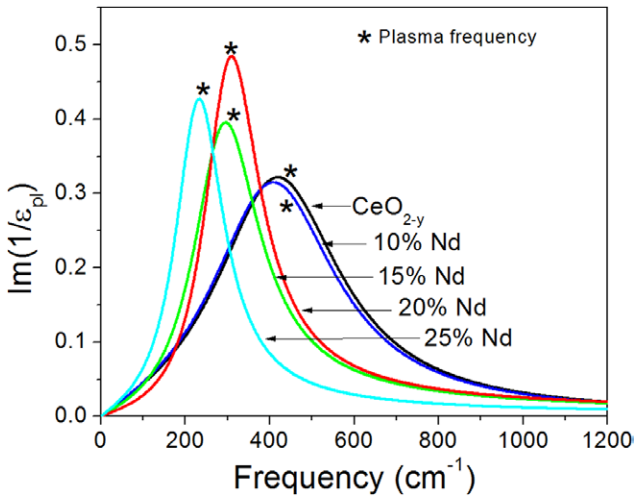

Figure 6. Decoupled plasmon mode structure in undoped and Nd doped samples. The positions of the plasma frequencies are marked with (*).

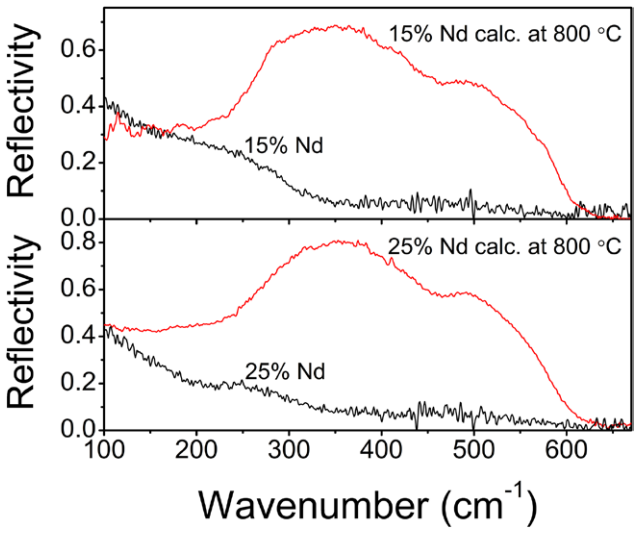

Figure 7. IR reflectivity spectra of untreated and thermally treated 15% (25%) Nd-doped samples.

mind that with temperature treatment in air, the nanosize effects become less pronounced with increasing crystallite size and that the concentration of the *F*-center defects and free carriers decreases.

Therefore, we can conclude that with increasing Nd content the plasmon–phonon interaction becomes stronger and at higher doping content (≥15% Nd) our samples undergo doping induced semiconductor–to–metallic state transition. With temperature treatment in air, it was demonstrated that the plasmonic background disappeared and the IR reflectivity spectra became similar to the bulk counterpart. The influence of doping on the n/m^* ratio and the estimation of the electron effective mass in pure and doped ceria nanocrystals will be the subject of our further work.

5. Conclusions

The influence of particle size decrease and Nd doping on the plasmon–phonon interaction in CeO_{2-y} nanocrystals was investigated. Analysis of the infrared reflection spectra of CeO_{2-y} nanocrystalline sample revealed that with decreasing of particle size the contribution of free charge carriers becomes significant, resulting in the appearance of the plasmon mode. The plasmon mode coupled strongly with two LO modes of ceria. The appearance of more pronounced low frequency Drude tail and screening of the phonon modes suggested that doping further increased the plasmon–phonon coupling. The plasmon–phonon interaction in undoped and doped CeO_{2-y} samples was investigated by using factorized and additive models combined with Bruggeman effective medium approximation. The factorized model based on plasmon-two LO phonon interaction has proven to fit the experimental data successfully. From this model, the coupled plasmon-LO phonon frequencies and dampings were derived. The application of the additive form for the dielectric function enabled to obtain decoupled LO phonon frequencies and to deduce about the decoupled plasmon mode structure. The red-shift of the plasmon mode, plasma damping decrease and

pronounced screening of the phonon modes with increasing Nd content in ceria nanocrystalline samples pointed out that doping induced semiconductor–to–metallic state transition took place.

Acknowledgments

This work was financially supported by the Serbian Ministry of Education, Science and Technological development under the projects ON171032 and III45018. The authors are also very grateful to the A von Humboldt Foundation for supporting this work.

References

[1] Nakamatsu H, Mukoyama T and Adachi H 1995 *Chem. Phys. Lett*. **247** 168
[2] Marabelli F and Wachter P 1987 *Phys. Rev.* B **36** 1238
[3] Steele B C H and Heinzel A 2001 *Nature* **414** 345
[4] Suzuki T, Funahashi Y, Yamaguchi T, Fujishiro Y and Awano M 2008 *J. Power Sources* **183** 544
[5] Knauth P 2006 *Solid State Ion.* **177** 2495
[6] Lapplainen J, Tuller H L and Lantto V 2004 *J. Electroceram.* **13** 129
[7] Tschöpe A, Bäuerle C and Birringer R 2004 *J. Appl. Phys*. **95** 1203
[8] Chiang Y-M, Lavik E B, Kosacki I, Tuller H L and Ying J Y 1996 *Appl. Phys. Lett.* **69** 185
[9] Suzuki T, Kosacki I, Anderson H U and Colomban P 2001 *J. Am. Ceram. Soc.* **84** 2007
[10] Jasinski P, Suzuki T and Anderson H U 2003 *Sensors Actuators B-Chem.* **95** 73
[11] Matović B, Dukić J, Devečerski A, Bošković S, Ninić M and Dohčević-Mitrović Z 2008 *Sci. Sintering* **40** 63
[12] Bošković S, Djurović D, Dohčević-Mitrović Z, Popović Z, Zinkevich M, Aldinger F 2005 *J. Power Sources* **145** 237
[13] Gervais F and Servoin J-L 1993 *Phys. Rev.* B **47** 8187
[14] Gonzalez R J, Zallen R and Berger H 1997 *Phys. Rev.* B **55** 7014
[15] Gervais F 1983 *Infrared and Millimeter Waves* vol 8 ed K J Button (New York: Academic) pp 279–339
[16] Kukharskii A A 1973 *Solid State Commun*. **13** 1761
[17] Kim O K and Spitzer G 1979 *Phys. Rev.* B **20** 3258
[18] Gervais F 2002 *Mater. Sci. Eng.* R **39** 29
[19] Webman I, Jortner J and Cohen M H 1977 *Phys. Rev.* B **15** 5712
[20] Spanier J E and Herman I P 2000 *Phys. Rev.* B **61** 10437
[21] Williamson G K and Hall W 1953 *Acta Metall*. **1** 22
[22] Zhou X-D and Huebner W 2001 *Appl. Phys. Lett.* **79** 3512
[23] Santha N I, Sebastian M T, Mohanan P, Alford N McN, Sarma K, Pullar R C, Kamba S, Pashkin A, Samukhina P and Petzelt J 2004 *J. Am. Ceram. Soc.* **87** 1233
[24] Chen Z W, Lai J K L and Shek C H 2006 *J. Non-Cryst. Solids* **352** 3285
[25] Skorodumova N V, Simak S I, Lundqvist B I, Abrikosov I A and Johansson B 2002 *Phys. Rev. Lett*. **89** 166601
[26] Han X, Lee J and Yoo H I 2009 *Phys. Rev.* B **79** 100403(R)
[27] Aškrabić S, Dohčević-Mitrović Z D, Araújo V D, Ionita G Jr, de Lima M M and Cantarero A 2013 *J. Phys. D: Appl. Phys*. **46** 495306
[28] Popović Z V, Dohčević-Mitrović Z D, Paunović N and Radović M 2012 *Phys. Rev.* B **85** 014302
[29] Chen Q and Wang J 2013 *Phys. Chem. Chem. Phys.***15** 17793
[30] Choudhury B and Choudhury A 2013 *Curr. Appl. Phys.* **13** 217
[31] Callan J P, Kim A M-T, Roeser C A D and Mazur E 2001 *Phys. Rev.* B **64** 073201
[32] Baumard J-F and Gervais F 1977 *Phys. Rev.* B **15** 2316
[33] Tajima S, Uchida S, Masaki A, Takagi H, Kitazawa K and Tanaka S 1985 *Phys. Rev.* B **32** 6302
[34] Goodenough J B and Cooper S L 2001 *Localized to Itinerant Electronic Transition in Perovskite Oxides* vol 98 ed J B Goodenough (Heidelberg: Springer-Verlag) pp 184–5
[35] Wu J, Walukiewicz W, Shan W, Yu K M, Ager J W III, Haller E E, Lu H and Schaff W J 2002 *Phys. Rev.* B **66** 201403